Impact of Bit Errors in Digitized RF Data on Ultrasound Image Quality

Chen, Zhao; Soozande, Mehdi; Vos, Rik; Bosch, Hans; Verweij, Martin; de Jong, Nico; Pertijs, Michiel

DOI
10.1109/TUFFC.2019.2937462

Publication date
2020

Document Version
Final published version

Published in
IEEE Transactions on Ultrasonics, Ferroelectrics and Frequency Control

Citation (APA)
Chen, Z., Soozande, M., Vos, R., Bosch, H., Verweij, M., de Jong, N., & Pertijs, M. (2020). Impact of Bit Errors in Digitized RF Data on Ultrasound Image Quality. *IEEE Transactions on Ultrasonics, Ferroelectrics and Frequency Control*, *67*(1), 13-24. Article 8812978. https://doi.org/10.1109/TUFFC.2019.2937462

Impact of Bit Errors in Digitized RF Data on Ultrasound Image Quality

Zhao Chen, *Member, IEEE*, Mehdi Soozande, *Student Member, IEEE*, Hendrik J. Vos, *Member, IEEE*, Johan G. Bosch, *Member, IEEE*, Martin D. Verweij, *Member, IEEE*, Nico de Jong, *Member, IEEE*, and Michiel A. P. Pertijs, *Senior Member, IEEE*

***Abstract*—This article quantitatively analyzes the impact of bit errors in digitized RF data on ultrasound image quality. The quality of B-mode images in both linear array and phased array imaging is evaluated by means of three objective image quality metrics: peak signal-to-noise ratio, structural similarity index, and contrast-to-noise ratio, when bit errors are introduced to the RF data with different bit-error rates (BERs). The effectiveness of coding schemes for forward error detection and correction to improve the image quality is also studied. The results show that ultrasound imaging is inherently resilient to high BER. The image quality suffers unnoticeable degradation for BER lower than 1E-6. Simple 1-bit parity coding with 9% added redundancy helps to retain similar image quality for BER up to 1E-4, and Hamming coding with 33.3% added redundancy allows the BER to increase to 1E-3. These results can serve as a guideline in the datalink design for ultrasound probes with in-probe receive digitization. With much more relaxed BER requirements than in typical datalinks, the design can be optimized by allowing fewer cables with higher data rate per cable or lower power consumption with the same cable count.**

***Index Terms*—Bit error rate (BER), datalink, forward error detection/correction (FEDC), image quality metrics (IQM), in-probe digitization.**

I. INTRODUCTION

IN CONVENTIONAL ultrasound probes, all transducer elements are individually connected to an imaging system using cables. This approach becomes impractical with the increase in the number of elements, e.g., in 2-D transducer arrays for 3-D imaging [1], [2]. Moreover, in the case of small elements with a relatively high electrical impedance, e.g., in catheter-based transducers, the cable load leads to significant attenuation, thus reducing the image quality [3], [4]. Integration of an application-specific integrated circuit (ASIC) in the probe head, capable of locally conditioning and processing the echo signals, is a solution that can address these issues [Fig. 1(a)]. By preprocessing the element-level echo signals, an ASIC allows the probe to use far fewer cable connections to the imaging system, thus enabling emerging miniature 3-D ultrasound probes which utilize high-density 2-D transducers (>1000 elements) and small-size catheters [1], [5], [6].

A variety of efforts have been made recently in ASIC designs for the reduction of cable count. A two-step beamforming scheme [7] is adopted in [1]. Local sub-array prebeamforming is realized through analog micro-beamformer circuits in the ASIC, leading to an order-of-magnitude cable-count reduction by only transferring the prebeamformed signals. In [9] and [10], the cable-count limitation is addressed by using analog time-division multiplexing (TDM) and frequency-division multiplexing (FDM), realizing eightfold and fourfold cable-count reductions, respectively.

The above-mentioned approaches all suffer from the inherent vulnerability of analog signals to crosstalk and interference and the design complexity of analog processing circuits. Recent studies have looked into utilizing local digital signal processing (DSP) in the ASICs [Fig. 1(b)], which requires in-probe digitization using a massively-parallel analog-to-digital converter (ADC) array [8], [11], [12]. Compared to analog approaches, in-probe digitization enables more robust digital data communication, allows high-speed wireline datalink technology to be leveraged to further reduce cable count and opens the path toward the use of optical and wireless links in future ultrasound devices.

However, to be able to adopt digital datalinks in future ultrasound probes, a deep understanding of the requirements of such datalinks becomes crucial. On the one hand, the datalink design is subject to stringent power constraints, especially for invasive ultrasound probes, in which in-probe power dissipation has to be limited to prevent tissue overheating [1]; on the other hand, the performance of the datalink, which is typically evaluated by the bit-error rate (BER), i.e., the ratio of the number of bit errors in a received bitstream and the total number of transmitted bits during a certain time interval, needs to be sufficient to minimize the impact of nonideal data transmission on the reconstructed ultrasound image quality.

The BER requirement for data communication is highly application-specific and may vary by several orders of magnitude. Very low BER is often required in intersystem data connections. For instance, 1000BASE-X requires a BER better

Manuscript received June 4, 2019; accepted August 21, 2019. Date of publication August 26, 2019; date of current version December 26, 2019. *(Corresponding author: Zhao Chen.)*

Z. Chen and M. A. P. Pertijs are with the Electronic Instrumentation Laboratory, Delft University of Technology, 2628 CD Delft, The Netherlands (e-mail: z.chen-3@tudelft.nl).

M. Soozande and J. G. Bosch are with the Department of Biomedical Engineering, Thoraxcenter, Erasmus Medical Center (Erasmus MC), 3015 CN Rotterdam, The Netherlands.

H. J. Vos, M. D. Verweij, and N. de Jong are with the Laboratory of Acoustical Wavefield Imaging, Delft University of Technology, 2628 CJ Delft, The Netherlands, and also with the Department of Biomedical Engineering, Thoraxcenter, Erasmus Medical Center (Erasmus MC), 3015 CN Rotterdam, The Netherlands.

Digital Object Identifier 10.1109/TUFFC.2019.2937462

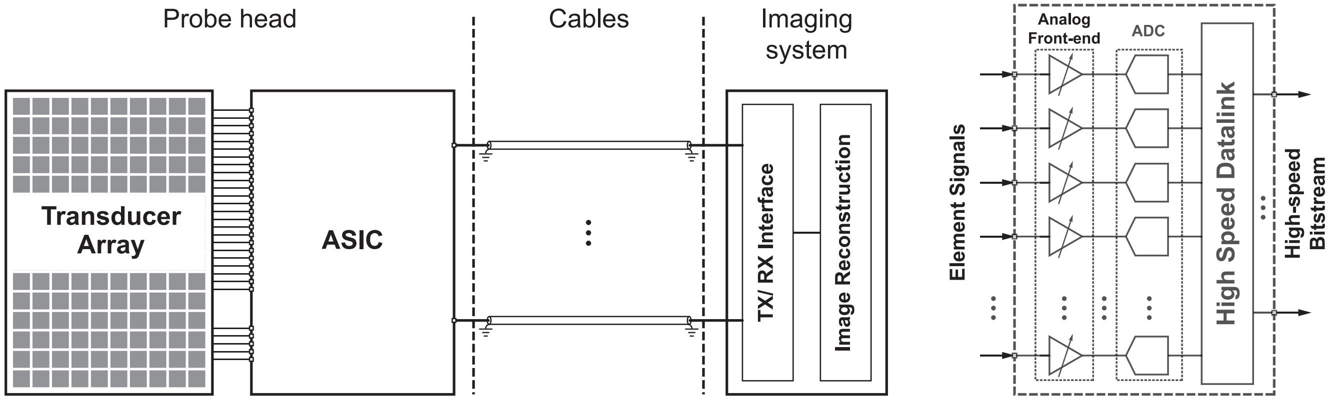

(a)

(b)

Fig. 1. (a) Block diagram of an ultrasound probe with in-probe ASIC. (b) Architecture of a receive ASIC with in-probe digitization.

than 1E-12, as defined by the IEEE 802.3 standard [13]. On the other hand, substantially higher BER levels are acceptable in some other applications, like telemetry in implantable devices for bio-potential recording. It has been reported in [14] that a BER below 2E-6 is sufficient to extract the spike information from recorded neural signals.

The BER requirements can have a significant impact on the power consumption of the datalink design and on the maximum data rate that can be supported by a cable, as will be discussed in Section II. However, the impact of bit errors on ultrasound imaging has not been studied much in detail. In [15] and [16], the impact of the BER on the quality of real-time echocardiogram transmission has been studied, but the transmitted data in this research are a series of reconstructed ultrasound images, not the RF data. A BER specification of 1E-5 has been reported for a wireless datalink in a capsule ultrasound imaging device [17], but without details regarding the motivation for this choice. In [18], a forward-looking IVUS probe with receive digitization has been reported with a BER of approximately 2E-3; however, the impact of the high BER on the reconstructed image quality has not yet been discussed.

This article investigates the impact of bit errors in digitized element-level RF signals on the reconstructed image quality. We propose a simulation setup to quantitatively assess image quality in the presence of bit errors based on the objective image quality metrics (IQM). Moreover, the efficiency of different coding schemes for data transmission is also studied. A minimum BER requirement is derived from the simulation results, which can guide the datalink design in future ultrasound probes.

This article is organized as follows. Section II discusses the factors affecting the BER in digital ultrasound probes. Section III introduces the proposed simulation setup for image quality analysis (IQA), followed by the simulation results in Section IV. Finally, Section V presents the discussions and conclusions.

II. BER IN DATA TRANSMISSION

The BER of a noise-limited communication system can be estimated from the ratio of the energy per bit and the noise power spectral density (E_b/N_0) in the receiver, where E_b is the signal energy associated with each data bit and N_0 is the noise power spectral density [19]. Fig. 2 shows the BER versus E_b/N_0 curve for data with two-level pulse amplitude modulation (2-PAM) transmitted across a channel with additive white Gaussian noise (AWGN), obtained in a MATLAB simulation (MathWorks, Inc., Natick, MA, USA). Though not all sources of bit errors can be considered as white noise, the curve is helpful to understand the relation between BER and E_b/N_0. Fig. 2 shows that E_b/N_0 reduces with the relaxation of the BER requirement. To achieve a BER of 1E-12, a minimum E_b/N_0 of 13.9 dB is required, while if the BER is relaxed to 1E-6, the required E_b/N_0 is also reduced to 10.5 dB.

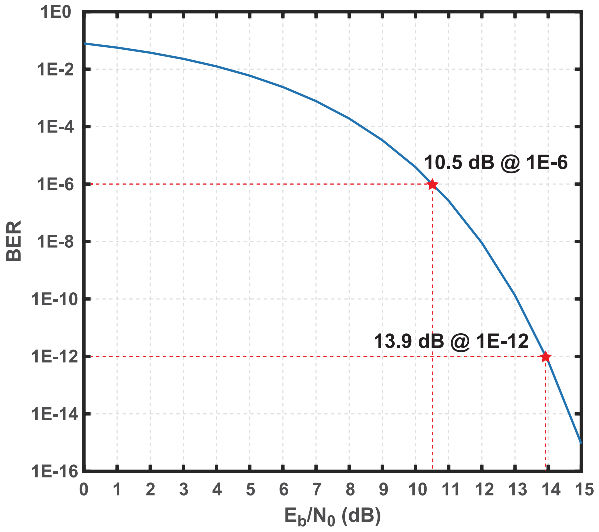

Fig. 2. BER versus E_b/N_0 plot for an AWGN channel with 2-PAM coded data.

Both E_b and N_0 are affected by the cascade of a transmitter, communication channel, and receiver. The nonideal channel is the most significant limiting factor of E_b/N_0 since the channel is typically subject to stringent physical constraints. Efforts need to be taken in the transmitter and receiver design to compensate the channel nonideality to achieve the required BER. A channel inevitably introduces channel loss and noise, causing an E_b/N_0 reduction. For wireline communication

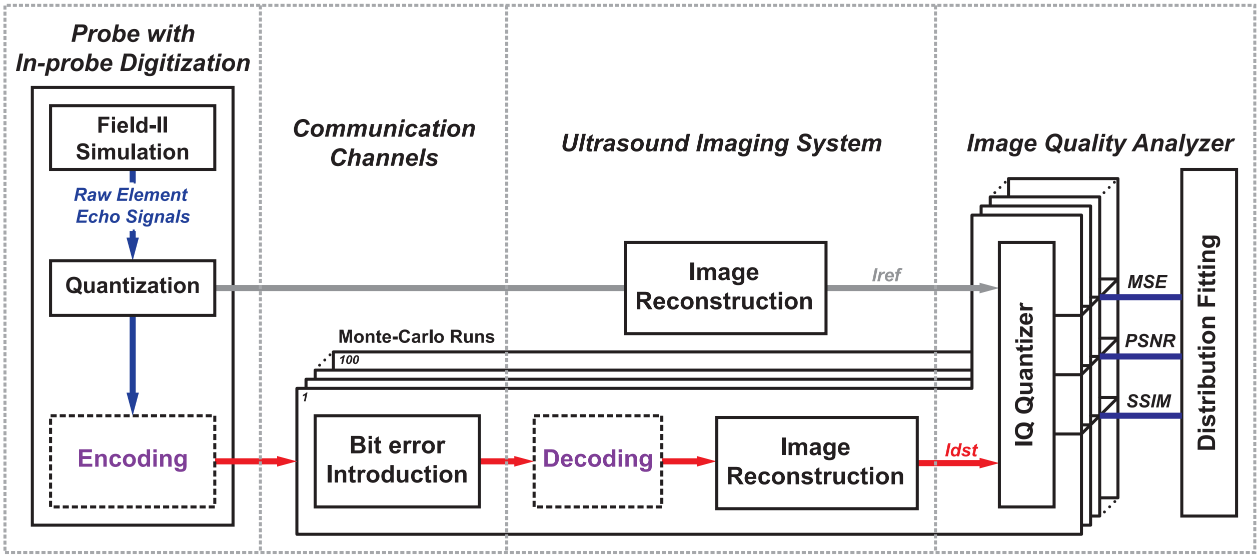

Fig. 3. Block diagram illustrating the simulation flow.

using cables as channels, channel loss becomes more significant at high frequency due to the cables' skin effect and dielectric losses [20]. Moreover, the channel dispersion introduces intersymbol interference (ISI), i.e., the phenomenon that a symbol transmitted across the cable is affected by the preceding symbol [21]. ISI is data-dependent and cannot be considered as white noise.

To minimize the impact of ISI, a typical method is to implement equalizer circuits in the transmitter and/or the receiver to compensate for the frequency response of the channel [22]. A communication system with sufficient equalization should guarantee that ISI does not dominate the BER performance, thus making the system noise-limited.

Although the BER performance is limited by E_b/N_0, forward error detection/correction (FEDC) coding can effectively reduce the impact of the error bits in the received data [21], [23]. FEDC adds redundant bits to the transmitted data and allows the receiver to detect and even correct a finite number of bit errors. FEDC is required in the existing 4-PAM standard improving the raw BER from 1E-6 to 1E-12 [24]. The BER mentioned in this article is the raw BER measured before the error correction in the receiver.

For catheter-based/endoscopic ultrasound imaging applications, the receivers will be implemented in the imaging system, where substantial computation power can be made available. In such a case, we can assume ISI can be fully compensated by complex equalizations in the receiver, making the system noise-limited. Then, it becomes crucial to know the BER requirement of the system to maximize the data rate per cable, or to minimize E_b/N_0, and eventually the in-probe power dissipation. For example, if a datalink is transmitting data at 0.9 Gbit/s across a 2-m Sumitomo cable (0.4DS-PBA, Sumitomo Electric) which has a nominal attenuation of 5 dB at 0.9 GHz and 8.4 dB at 2 GHz, according to Fig. 2, when relaxing the BER requirement from 1E-12 to 1E-6, a designer can either increase the data rate to 2 Gbit/s on the cable, or, with the same data rate, reduce the transmit power by 3.4 dB, saving half of the power consumed in the probe for data transmission.

III. EVALUATION METHODS

A. Overview

We have performed a MATLAB simulation to emulate the proposed ultrasound system consisting of an ultrasound probe with receive digitization, a datalink, and back-end image reconstruction. Fig. 3 illustrates the simulation flow: raw element echo signals are acquired from a simulation using the ultrasound simulation tool Field-II [25], [26] on a transducer with a predefined phantom and then quantized and encoded in a binary format; bit errors are randomly introduced to the binary data with prescribed BER levels; a reference image I_{ref} and distorted images I_{dst} are reconstructed from the binary data before and after the bit-error introduction, respectively; finally, objective IQMs are calculated from a 100-run Monte Carlo simulation to evaluate the image quality of the distorted images. If FEDC is enabled, extra encoding and decoding steps are applied to the binary data before and after the introduction of the bit errors. The effectiveness of FEDC on image quality improvement can be analyzed by turning on and off this option.

B. Raw Echo Data Acquisition

As representative case studies, a linear array transducer and a phased array transducer, both with 128 elements, have been simulated using Field-II. The methodology can also be applied to other transducers with different array sizes and array configurations, such as 2-D transducers.

Both transducers have a center frequency of 5 MHz and a fractional bandwidth of 100%. The element pitches of the linear and phased array transducers are one wavelength and half wavelength of the center frequency, respectively. The parameters of the two transducers are listed in Table I.

TABLE I
SIMULATION PARAMETERS FOR BOTH THE LINEAR ARRAY AND PHASED ARRAY TRANSDUCERS IN FIELD II

	Linear Array	**Phased Array**
No. of elements	128	128
Center frequency	5 MHz	5 MHz
Wavelength (λ)	308 μm	308 μm
Element pitch	λ	λ / 2
Element width	0.9 × λ	0.9 × λ / 2
Kerf	0.1 × λ	0.1 × λ / 2
Element height	5 mm	5 mm

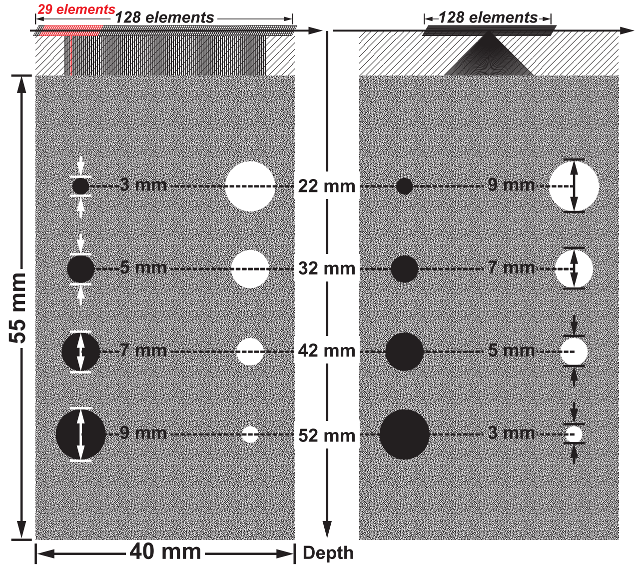

a). Linear Array Transducer b). Phased Array Transducer

Fig. 4. Imaging phantom and its positioning in the Field-II simulation.

We have created a 2-D simulation phantom with a size of 40 mm × 55 mm, positioned at 10 mm from the surface of the transducers, composed of 150 000 (6.5 per wavelength) randomly distributed scatterers (Fig. 4). The region between the transducer and the phantom (marked by slash lines) is acoustically transparent. Four hyperechoic and four anechoic circular regions with different diameters are placed 10 mm away from the center of the phantom at different depths (from 22 to 52 mm, with a step of 10 mm), marked by the white and black circles in Fig. 4. All depths are measured from the transducer surface. The amplitudes of the scatterers, representing the return echo intensities, are set to 10 and 0 in the hyperechoic and anechoic regions, respectively; the amplitudes of the background scatterers are randomly set, following a Gaussian distribution with a mean of 0 and a standard deviation of 1.

For the linear array transducer, 29 elements are active in each pulse-echo simulation, and for the phased array transducer, all elements are active to steer beams from −45° to 45° with an angular step of 0.91°, thus forming 100 scanlines across the aperture in both cases. A fixed transmit focus point is placed at a depth of 50 mm, while multiple focal points at a depth from 10 to 65 mm, with a step of 5 mm are used in receive. The active elements are excited by a two-cycle sinusoidal burst in transmit. Hamming apodization is applied in both transmit and receive. The sampling frequency in reception is set to 20 MS/s, 4 × the transducers' center frequency. The calculated raw element echo signals are acquired and stored in two data sets. Each point in these data sets indicates a sample of the element-level echo signals. Propagation attenuation is not taken into account in the simulation for simplicity since it is assumed that attenuation will be fully compensated for by time–gain compensation in the analog front end before analog-to-digital conversion, thus leading to similar echo signals. The signals are digitized to binary data with 10-bit resolution across their full signal swing.

C. Bit-Error Introduction

The random bit-error introduction is realized by feeding the binary data into a noisy binary symmetric channel. The channel randomly introduces bit errors according to the predefined channel error probability, which is an accurate approximation of the channel BER when the data set is large enough. We use six discrete BER levels from 1E-6 to 1E-1 for this simulation, one level per decade.

D. Error Detection and Correction

Different FEDC schemes can be applied to the binary data to improve its immunity to bit errors. Since the encoding should be done in the probe, a simple and low-power hardware implementation of the encoding scheme is crucial. Moreover, stronger error detection/correction capability often requires more redundancy. Powerful encoding schemes improve the received BER at the cost of a reduction of the effective data rate per channel unless a higher bit rate is adopted. A lower effective data rate implies that more cables will be needed, while a higher bit rate translates into higher power consumption to keep the same BER. The tradeoff between error detection/correction capability and redundancy needs to be carefully considered when choosing a suitable encoding scheme in the ultrasound probe design. The simulation should take this tradeoff into account.

Two types of FEDC schemes, parity checking [27] and Hamming coding [28], have been used in the simulation. Parity checking can detect any odd number of bit errors in a string of binary data. It is the simplest error-detection code in terms of hardware implementation which adds only one redundant bit, but parity cannot detect an even number of bit errors and is not capable of correcting the detected errors. Hamming coding uses more than one parity bit in a string of binary data and arranges them in a way that error bits at different locations produce unique parity-check results. By adding more redundant bits to a string of binary data, Hamming coding enables not only the detection of bit errors but also the correction of single-bit errors [28].

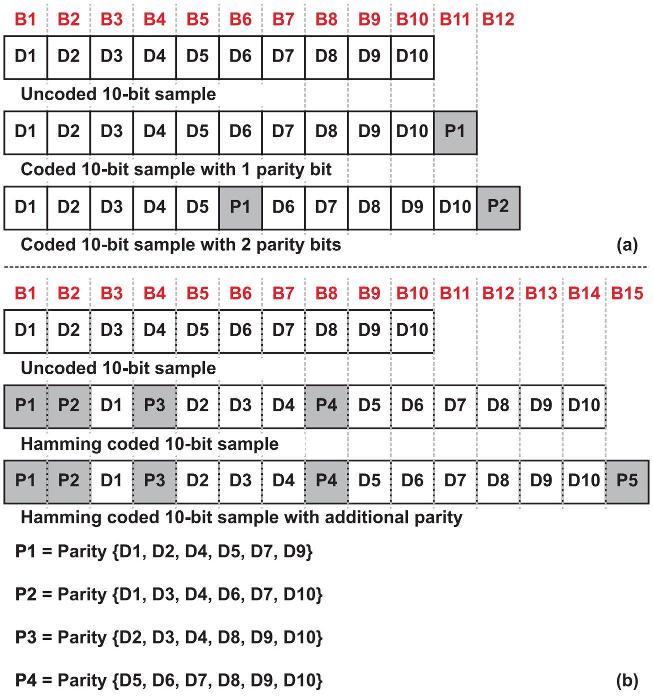

Fig. 5. Illustrations of the FEDC schemes. (a) Parity checking. (b) Hamming coding.

Since the echo signals are digitized with 10-bit resolution, the FEDC encoding is also applied to every 10-bit binary sample. Fig. 5 shows different encoding schemes that have been applied.

Parity coding extends a 10-bit sample (D10–D1) to 11 or 12 bits by adding an even parity bit in every 10 or 5 bits, as shown in Fig. 5(a). The effective transmission rate in the two cases is 90.9% and 83.3%, respectively.

Hamming coding extends a 10-bit binary sample to 14 bits by adding four redundant bits (P1–P4), and P1–P4 are the parity bits of the specific bits in the 10-bit binary sample [Fig. 5(b)].

Any single-bit error in the coded 14-bit data produces a unique combination of P1–P4, thus allowing the decoder to identify the locations of the single-bit errors and to correct them [28]. However, the error detection and correction will fail if the coded data contain multi-bit errors. Since the evaluated BER range is from 1E-6 to 1E-1, there is still a large probability that multi-bit errors, especially dual-bit errors, appear in the coded 14-bit data. An additional parity bit (P5) is added to enable dual-bit error detection. P5 is the even parity bit of all the data bits (D10–D1) and parity bits (P4–P1). The combination of P5 and P1–P4 detects dual-bit errors and corrects single-bit errors. Then, the effective transmission rate of the Hamming coding is 71.4% and 66.7%, in cases w/ and w/o the global parity bit.

The data with bit errors are first decoded before image reconstruction on a sample-by-sample basis if FEDC is enabled. Parity bits are separated from the data bits and sent to a parity checker. For coding with only a parity-check bit, samples which fail the parity check are discarded and replaced by 0. For Hamming coding, if a sample fails both the parity check of P1–P4 and P5, the error in the sample is considered as a single-bit error and the error bit is flipped; if a sample only fails the parity check of P5, the error is considered as a single-bit error at P5 and the sample is considered as error-free; while if a sample only fails the parity check of P1–P4, the error in the sample is considered as a dual-bit error and the sample is discarded. The error-corrected 10-bit data are converted to a decimal format for image reconstruction.

E. Image Reconstruction

The image reconstruction uses simple delay-and-sum beamforming. The beamformed data B at the kth time sample are calculated by

$$B(k) = \frac{N}{N - N_{\mathrm{err}}} \times \sum_{i=1}^{N} S_i(k) \tag{1}$$

where N and N_{err} are the total number of samples and the number of error samples in one beamforming operation, respectively, and S_i is the delayed echo signal of the ith element. Since, as mentioned, samples with detected errors have been replaced by zeros, this expression effectively represents a beamforming operation on the $(N - N_{\mathrm{err}})$ correct samples. Envelopes extracted from the beamformed data are logarithmically compressed and then displayed on a 50-dB gray-scale image. The dynamic range of the envelopes is limited to 100 dB, with respect to the maximum value in the reference image, for the following IQM calculations.

F. Image Quality Analysis

Since a reference image can be constructed from the raw error-free element echo data, a full-reference IQA can be performed. Three full-reference IQMs are adopted in the evaluation: peak-signal-to-noise ratio (PSNR), structural similarity (SSIM), and contrast-to-noise ratio (CNR).

PSNR is calculated as the ratio between the maximum pixel power in a reference image and the mean-squared error (MSE) of a distorted image, where MSE is defined as the averaged squared difference between the values of the pixels in the reference image and in a distorted image [29]. For reference image R and distorted image D consisting of $m \times n$ pixels, the equations of PSNR and MSE are given as follows:

$$\mathrm{PSNR} = 10 \cdot \log_{10} \frac{[\max(R)]^2}{\mathrm{MSE}} (2) \tag{2}$$

and

$$\mathrm{MSE} = \frac{1}{m \cdot n} \sum_{i=1}^{m} \sum_{j=1}^{n} [R(i, j) - D(i, j)]^2. \tag{3}$$

PSNR is one of the most widely used IQM for full-reference IQA because it is simple to calculate, has clear physical meaning, and is mathematically convenient for image quality optimization [30]. However, in some cases, it shows low correlation with the perceptual quality of the distorted images, especially for ultrasound images in which significant speckle noise exists [31].

In contrast to statistical metrics like MSE and PSNR, SSIM is based on human visual perception. It has been used in several studies on the quality assessment on medical ultrasound

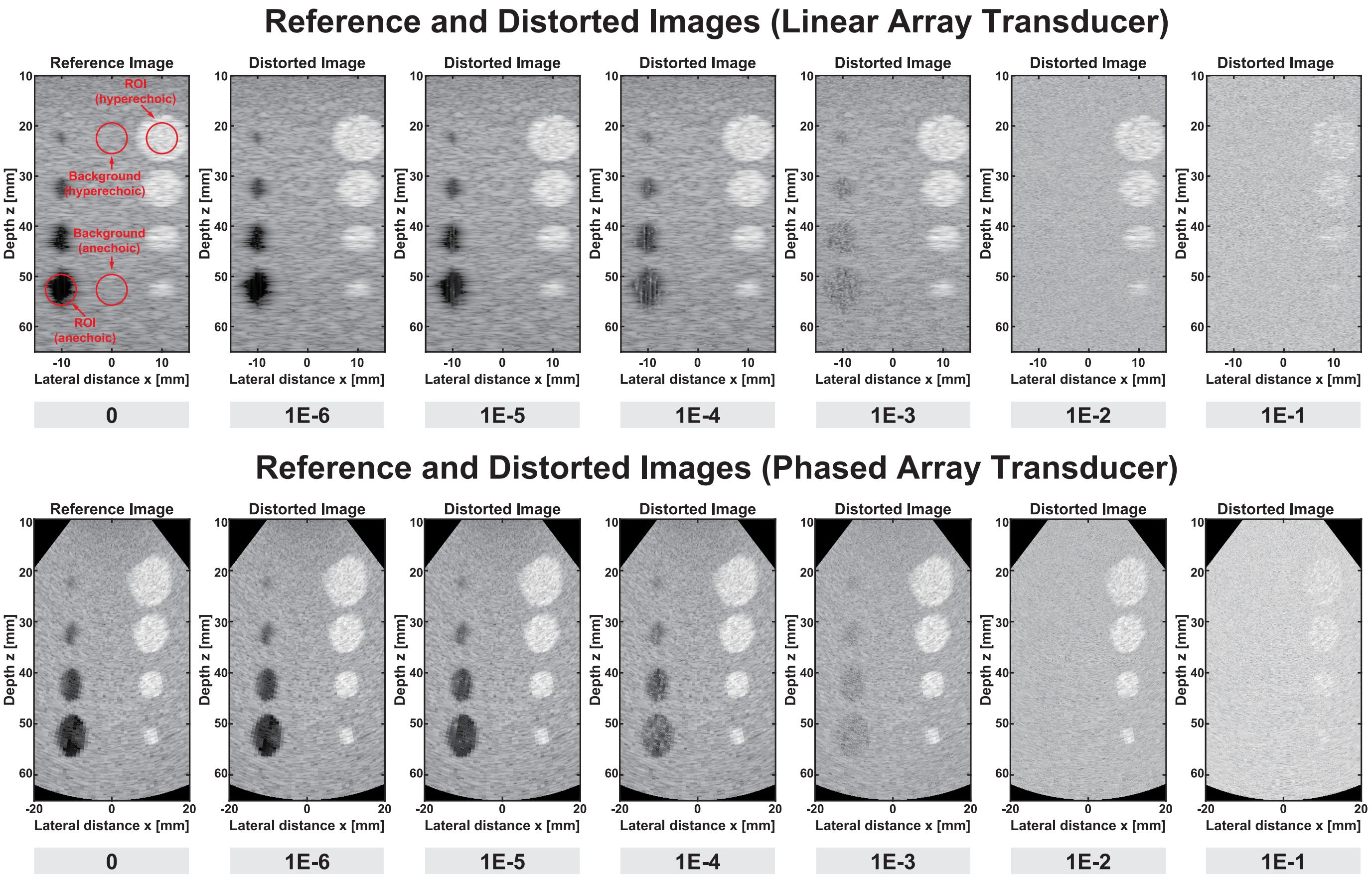

Fig. 6. Reference and distorted images for both linear array and phased array transducers at different BER levels (without error detection or correction).

videos and shows good correlation with the subjective score provided by medical experts [31]. The computation of the SSIM index is based on a multiplication of three terms: a luminance term, a contrast term, and a structural term [30]. For a reference image R and a distorted image D, SSIM is calculated as follows:

$$\mathrm{SSIM} = \frac{(2\mu_R \cdot \mu_D + C_1)(2\sigma_{RD} + C_2)}{\left(\mu_R^2 + \mu_D^2 + C_1\right)\left(\sigma_R^2 + \sigma_D^2 + C_2\right)} \tag{4}$$

where μ_R, μ_D, σ_R, σ_D, and σ_{RD} are the means, standard deviations, and cross-covariance of the two images, C_1 and C_2 are two constants $\ll 1$ to avoid instability for $\mu_R = \mu_D = 0$ and $\sigma_R = \sigma_D = 0$.

Another widely used IQM in medical ultrasound imaging is CNR [32]. It is used to quantify the detectability of a region of interest (ROI), normally a cyst, from its background, and is typically calculated by [33]

$$\mathrm{CNR} = \frac{|\mu_{\mathrm{ROI}} - \mu_{\mathrm{bg}}|}{\sqrt{\sigma_{\mathrm{ROI}}^2 + \sigma_{\mathrm{bg}}^2}} \tag{5}$$

where μ_{ROI}, μ_{bg}, and σ_{ROI}, σ_{bg} are the means of the image pixel intensity inside the ROI and in the background, and the standard deviations of the image pixel intensity inside the ROI and in the background, respectively. The pixel intensity used in the CNR calculation is after logarithmic compression [34]. Since CNR quantifies the contrast between two regions in one image, the impact of BER is evaluated by the CNR degradation between the distorted image and the reference image.

Since the bit errors are randomly introduced to the binary data, bit errors occurring at the most-significant bit (MSB) and at the least-significant bit (LSB) of a sample will have a significantly different impact on the calculated PSNR and SSIM values. Furthermore, the distortions due to bit errors will only influence the calculated CNR when they are appearing in an ROI in distorted images. To obtain representative values for the IQMs despite this varying impact of bit errors, we perform a 100-run Monte Carlo simulation and obtain IQM estimates from the statistics of sets of distorted images produced. The reliability of the results is reflected by the confidence intervals of the IQM estimates.

IV. SIMULATION RESULTS

The reference image I_{ref} is directly reconstructed from the digitized raw element echo signals, without bit errors. A set of distorted images $I_{\mathrm{dst}}\langle 1:6\rangle$ is reconstructed from the error data with BER levels from 1E-1 to 1E-6, when FEDC is OFF. Fig. 6 shows I_{ref} (left-most images) and $I_{\mathrm{dst}}\langle 1:6\rangle$ for both linear array and phased array transducers.

For $I_{\mathrm{dst}}\langle 1:6\rangle$ in both linear array and phased array imaging, when the BER is 1E-2 or higher, only the hyperechoic regions can still be distinguished, while the anechoic regions and the background are below the noise floor; when the BER level

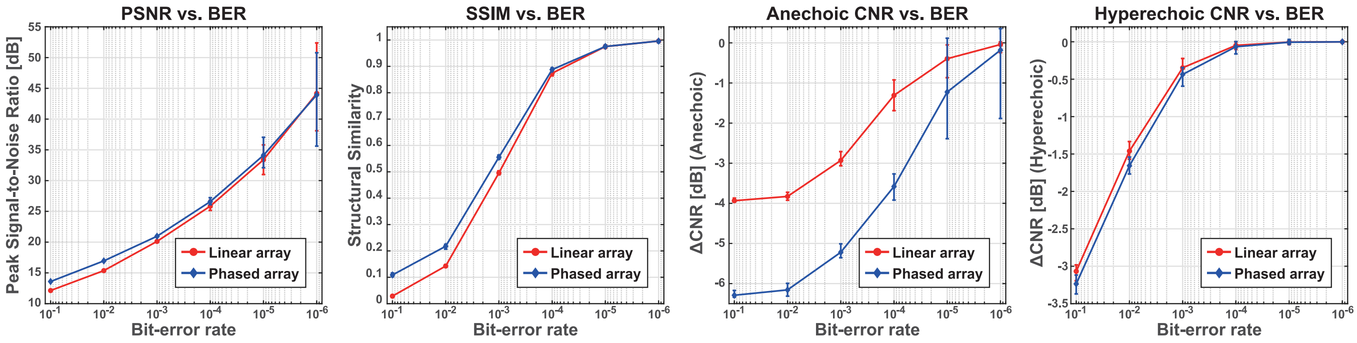

Fig. 7. IQM versus BER plots for images from both linear array and phased array transducers (without error detection or correction).

goes down to 1E-3–1E-5, both the hyperechoic and anechoic regions can be distinguished, but erroneous pixels are still easily visible in the anechoic regions; when the BER level is further reduced to 1E-6, the distorted image is almost the same as the reference image.

The statistics of PSNR, SSIM, and CNR degradation ($\mathrm{CNR}_{\mathrm{dst}} - \mathrm{CNR}_{\mathrm{ref}}$) between $I_{\mathrm{dst}}\langle 1:6\rangle$ and I_{ref} are derived from a 100-run Monte Carlo simulation. CNR degradations for both hyperechoic and anechoic regions are calculated. The ROI and background regions for CNR calculation are marked in Fig. 6. The calculated IQMs can be plotted using the mean values of the Monte Carlo results. The PSNR can be very well represented by their mean values (μ) at high BER levels, since the high BER leads to a small relative standard deviation (σ/μ). However, when BER is lower ($\leq$ 10E-5), the large relative standard deviation makes the mean values less representative for the expected image quality. Therefore, we display the IQMs in error-bar plots, where the upper and lower bounds are the maximum and minimum values in the 100 runs, allowing the IQMs at low BER levels to be estimated using the worst-case values in the plots.

Fig. 7 shows the error-bar plots of the five IQMs versus BER for both the linear array and phased array imaging. The trends of the IQM curves are in good agreement with the image quality observed in Fig. 6. For the unacceptable images (BER $>$ 1E-2), we get PSNR $<$ 20 dB and SSIM $<$ 0.25, respectively. The CNR degradations in hyperechoic region and anechoic region are over -3.5 and -1.5 dB, respectively. For images with no visible distortions (BER $<$ 1E-6), we get PSNR $>$ 40 dB and SSIM $>$ 0.99, and the CNR degradations are very close to 0. In contrast with most telecommunication applications, which normally require BER levels better than 1E-12–1E-15 [35]–[37], the quality of the reconstructed ultrasound images remains high at BER $<$ 1E-6.

When FEDC is ON, four distorted images $I_{\mathrm{dst\_}a}$, $I_{\mathrm{dst\_}b}$, $I_{\mathrm{dst\_}c}$, and $I_{\mathrm{dst\_}d}$ are reconstructed from the data coded by: 1) one parity bit; 2) two parity bits; 3) Hamming code; and 4) Hamming code with one additional parity bit. The distorted images together with the reference image from the phased array transducer at different BER levels are shown in Fig. 8.

Visually, the image quality of the four distorted images at BER = 1E-1 does not differ from the image quality of I_{dst} in Fig. 6. However, when BER reduces to 1E-2, all four images with FEDC show much more distinguishable anechoic regions from the background, compared with I_{dst}. I_{dst_d} shows the best image quality, though several defective pixels can still be observed in the anechoic regions. When the BER level is further reduced to 1E-3, hardly any difference can be seen between $I_{\mathrm{dst\_}d}$ and the reference image, while $I_{\mathrm{dst\_}a}$, $I_{\mathrm{dst\_}b}$, and $I_{\mathrm{dst\_}c}$ show similar image quality. All the images at BER level of 1E-4 or better are almost the same as the reference image.

Fig. 9 shows the error-bar plots of the IQMs of the four images with FEDC versus BER for both the linear array and phased array imaging. PSNR values higher than 58 dB are rounded to 58 dB, to be better displayed in the plots. $I_{\mathrm{dst\_}d}$ outperforms all others in all the IQMs in both linear array and phased array images when BER is better than 1E-2. When BER is better than 1E-4, the PSNR values of all the four distorted images are $>$ 45 and the SSIM and CNR degradations are also very close to their theoretical limits. This is also well aligned with the visual perception of the images in Fig. 8.

The effectiveness of the encoding is quantitatively evaluated by comparing the IQMs of the unencoded data image I_{dst} and the four encoded data images in Figs. 7 and 9. At BER = 1E-1, there is no significant difference among the five distorted images. Encoding is not effective at very high BER levels. This can be expected because the data encoding is applied in every 10-bit sample. For example, BER = 1E-1 implies that the majority of the samples contain bit errors and are discarded in the image reconstruction. The images are reconstructed from the remaining insufficient data samples. At BER = 1E-2, encoding significantly improves the three IQMs for all the four encoded data images, especially for $I_{\mathrm{dst\_}d}$. The PSNR and SSIM of $I_{\mathrm{dst\_}d}$ using Hamming coding and 1-b parity are $>$ 25 dB and $>$ 0.88, respectively, which are already better than the metrics of I_{dst} obtained at BER = 1E-4. The degradation of CNR for hyperechoic regions is almost negligible. However, the degradation of CNR for anechoic regions in phased array imaging is over 3 dB. When BER $\leq$ 1E-4, we have PSNR $>$ 45 dB, SSIM $>$ 0.97, and there is virtually no CNR degradation for all the four distorted images, while the BER level needs to be reduced to 1E-6 for I_{dst} to have similar results.

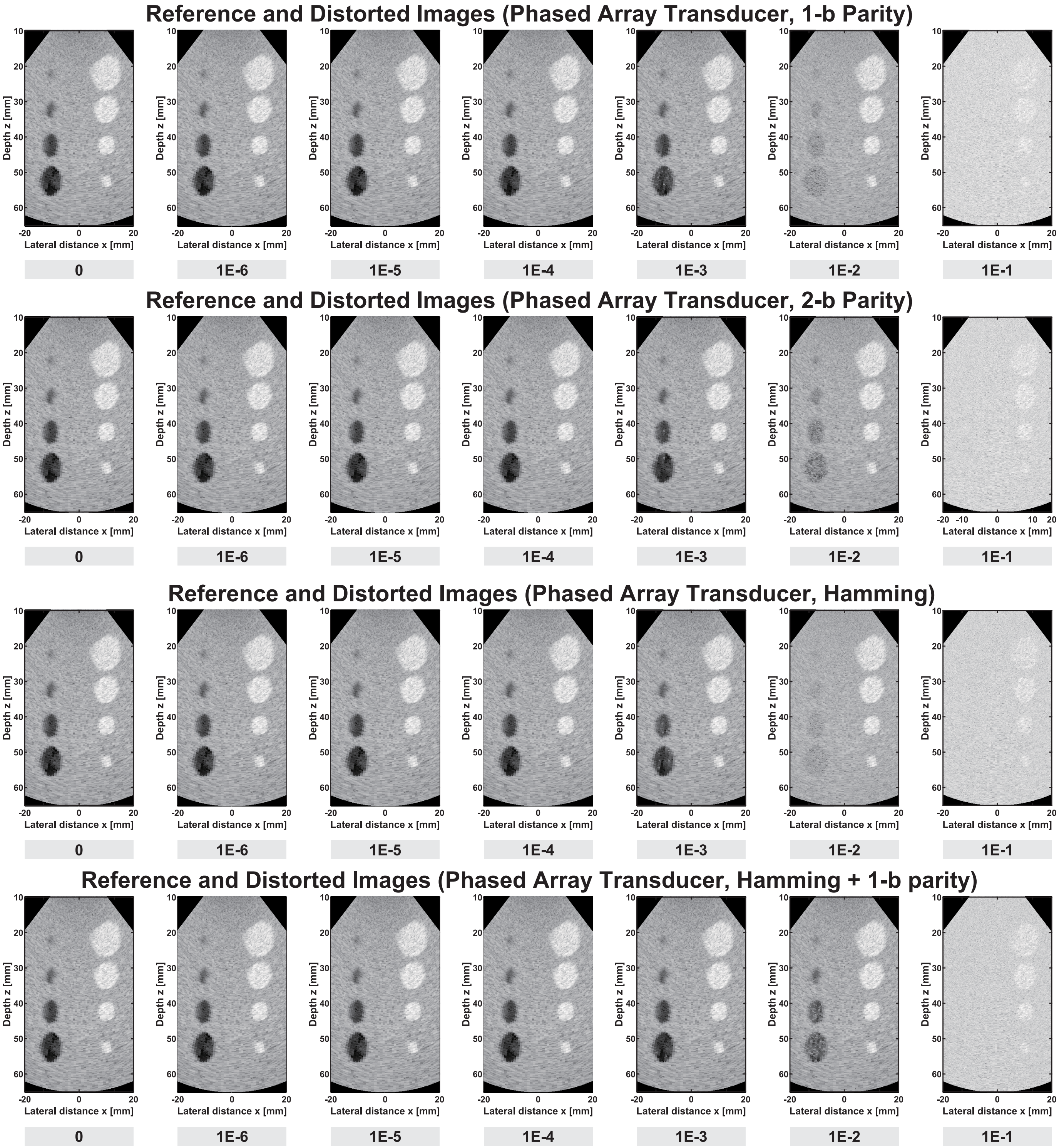

Reference and Distorted Images (Phased Array Transducer, 1-b Parity)

Reference and Distorted Images (Phased Array Transducer, 2-b Parity)

Reference and Distorted Images (Phased Array Transducer, Hamming)

Reference and Distorted Images (Phased Array Transducer, Hamming + 1-b parity)

Fig. 8. Reference and distorted images for phased array transducers at different BER levels, with error detection using parity bits and error detection and correction using the Hamming coding.

Though the encoding is not beneficial to the image quality when the BER is very high or very low, it effectively relaxes the BER requirement by roughly two orders of magnitude when the BER is between 1E-2 and 1E-5. For images reconstructed from data with the Hamming coding, the image quality at BER = 1E-3 is still very high; even for images reconstructed from data with simple 1-bit parity coding, a comparable image quality can be obtained at BER = 1E-4.

To verify whether the conclusions can be applied to more complex images, we adopt an artificial phantom for a 3-month fetus [38] in the simulation. A reference image and four distorted images from unencoded data at BER = 1E-6, 1-bit parity coded data at BER = 1E-4, Hamming coded data with

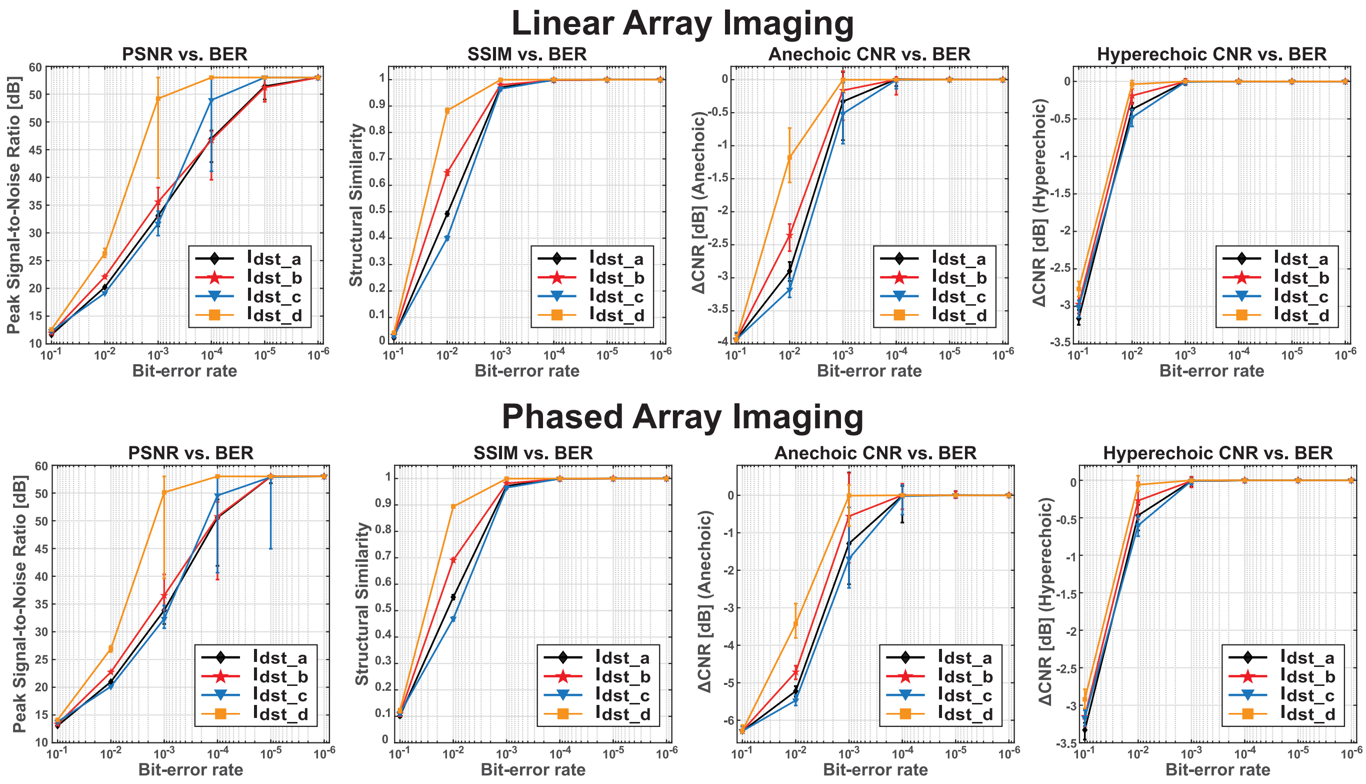

Fig. 9. IQM versus BER plots for images from both linear arrayand phased array transducers (with error detection or correction).

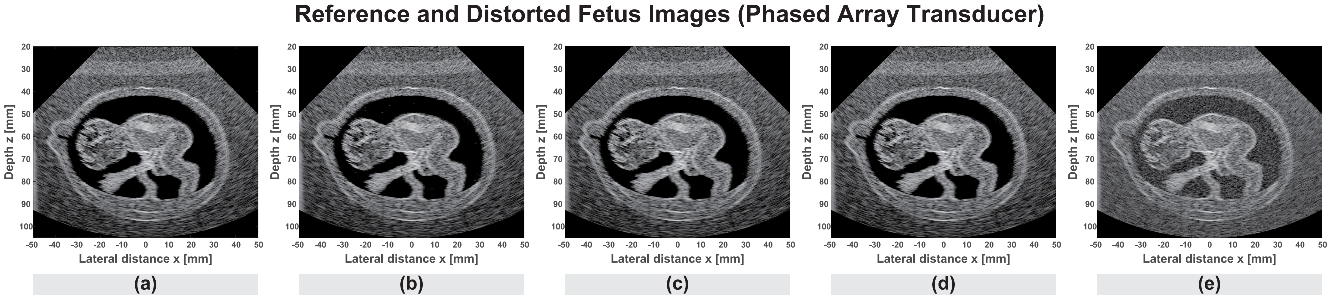

Fig. 10. (a) Reference fetus image and four distorted images from data. (b) Without error detection or correction, BER = 1E-6. (c) With 1-bit parity coding, BER = 1E-4. (d) With Hamming coding with additional parity bit, BER = 1E-3. (e) Without error detection or correction, BER = 1E-3.

TABLE II

IQM VALUES OF THE FOUR DISTORTED FETUS IMAGES IN FIG. 10

Distorted Images			IQM	
	Coding	BER	PSNR	SSIM
(b)	*No coding*	*1E-6*	*46.63*	*0.9978*
(c)	*1-b Parity coding*	*1E-4*	*54.08*	*0.9996*
(d)	*Hamming coding + 1-b parity*	*1E-3*	*47.74*	*0.9987*
(e)	*No coding*	*1E-3*	*17.61*	*0.5987*

additional parity bit at BER = 1E-3, and unencoded data at BER = 1E-3 are shown in Fig. 10(a)–(e), respectively. The imaging artefacts due to the high BER can be clearly observed in Fig. 10(e). When reducing the BER to 1E-6, the distorted images [Fig. 10(b)] are almost identical to the reference image [Fig. 10(a)]. Similar image quality can also be obtained by proper data coding, even when the BER remains high. The IQM of the distorted images is shown in Table II. The PSNR and SSIM of images [Fig. 10(b)–(d)] are over 45 dB and 0.995, respectively, a lot better than the 17.61 dB and 0.6 of image [Fig. 10(e)], which indicates that the distorted images from coded data are indeed very close to the reference image despite the high BER levels.

V. DISCUSSION AND CONCLUSION

We have built a simulation model to quantitatively evaluate the quality of B-mode ultrasound images reconstructed from digitized element-level RF echo signals with different BER levels. According to the simulation results shown in Section IV, ultrasound images show inherent resilience to BER levels which are typically unacceptable in digital communication. The image quality, which is quantified by PSNR, SSIM, and CNR, shows unnoticeable degradation for BER levels lower than 1E-6. Unlike other applications which can also be immune to high BER but require complex encoding algorithms [16], simple coding schemes with low hardware cost prove to be very efficient for ultrasound imaging in further improving the immunity to bit errors. Simple 1-bit parity coding with 9% added redundancy helps to retain similar image quality for BER up to 1E-4, and Hamming coding with 33.3% added redundancy allows the BER to increase to 1E-3.

The inherent resilience to bit errors is due to the averaging effect in beamforming. At high BER levels, where the bit errors can be modeled as a Gaussian-distributed noise superimposed to the raw element data, the beamforming operation effectively reduces the noise power by a factor of N, where N is the number of elements involved in the beamforming, thus reducing the impact of a bit error on the final image. At high BER levels, phased array imaging is more resilient to bit errors compared to a linear array transducer with the same number of elements, since the receive beamforming in a phased array system involves the echo signals of all the elements in the array, not a subset of the elements, thus resulting in a larger N. However, if the aperture in a linear array imaging is expanded to the point where all elements are involved, a similar image quality is expected from both linear array and phased array imaging.

The resilience to bit errors can be further enhanced by compounding multiple consecutive B-mode images in the time domain, which is commonly used to improve the ultrasound image quality. Similar to the spatial beamforming in a single frame, the inherent averaging effect in a compounding operation can also be effective in suppressing the image artifacts due to bit errors. By enabling averaging in both the spatial and time domains, real-time ultrasound images are likely to tolerate higher BER than static B-mode images, which are already proven to be quite immune to bit errors.

This work has focused on the impact of bit errors on B-mode envelope-processed images. Future work will include extending the study to Doppler imaging, where the phase information of the RF data, rather than the envelope of the beamformed data, is of more importance.

The conclusion of this work can serve as a guideline in the datalink design of ultrasound probes with in-probe receive digitization. The simulation results reveal that a nonstandard datalink design with relatively poor BER performance (>1E-6) can be quite acceptable for ultrasound imaging applications. This allows the datalink to operate at a higher data rate per cable, thus reducing the number of cables required, or to operate at the same data rate per cable, while reducing the overall power consumption.

REFERENCES

[1] C. Chen *et al.*, "A prototype PZT matrix transducer with low-power integrated receive ASIC for 3-D transesophageal echocardiography," *IEEE Trans. Ultrason., Ferroelectr., Freq. Control*, vol. 63, no. 1, pp. 47–59, Jan. 2016.

[2] J. Janjic *et al.*, "A 2-D ultrasound transducer with front-end ASIC and low cable count for 3-D forward-looking intravascular imaging: Performance and characterization," *IEEE Trans. Ultrason., Ferroelectr., Freq. Control*, vol. 65, no. 10, pp. 1832–1844, Oct. 2018.

[3] I. O. Wygant *et al.*, "An integrated circuit with transmit beamforming flip-chip bonded to a 2-D CMUT array for 3-D ultrasound imaging," *IEEE Trans. Ultrason., Ferroelectr., Freq. Control*, vol. 56, no. 10, pp. 2145–2156, Oct. 2009.

[4] I. Cicek, A. Bozkurt, and M. Karaman, "Design of a front-end integrated circuit for 3D acoustic imaging using 2D CMUT arrays," *IEEE Trans. Ultrason., Ferroelectr., Freq. Control*, vol. 52, no. 12, pp. 2235–2241, Dec. 2005.

[5] E. Kang *et al.*, "A reconfigurable ultrasound transceiver ASIC with24 × 40elements for 3-D carotid artery imaging," *IEEE J. Solid-State Circuits*, vol. 53, no. 7, pp. 2065–2075, Jul. 2018.

[6] Y. Katsube *et al.*, "Single-chip 3072ch 2D array IC with RX analog and all-digital TX beamformer for 3D ultrasound imaging," in *IEEE ISSCC Dig. Tech. Papers*, vol. 60, Feb. 2017, pp. 458–459.

[7] B. Savord and R. Solomon, "Fully sampled matrix transducer for real time 3D ultrasonic imaging," in *Proc. IEEE Symp. Ultrason.*, Oct. 2003, pp. 945–953.

[8] C. Chen *et al.*, "A pitch-matched front-end ASIC with integrated subarray beamforming ADC for miniature 3-D ultrasound probes," *IEEE J. Solid-State Circuits*, vol. 53, no. 11, pp. 3050–3064, Nov. 2018.

[9] T. M. Carpenter, M. W. Rashid, M. Ghovanloo, D. M. J. Cowell, S. Freear, and F. L. Degertekin, "Direct digital demultiplexing of analog TDM signals for cable reduction in ultrasound imaging catheters," *IEEE Trans. Ultrason., Ferroelectr., Freq. Control*, vol. 63, no. 8, pp. 1078–1085, Aug. 2016.

[10] M. W. Rashid, C. Tekes, M. Ghovanloo, and F. L. Degertekin, "Design of frequency-division multiplexing front-end receiver electronics for CMUT-on-CMOS based intracardiac echocardiography," in *Proc. IEEE Int. Ultrason. Symp.*, vol. 1, Sep. 2014, pp. 1540–1543.

[11] M. C. Chen *et al.*, "A pixel pitch-matched ultrasound receiver for 3-D photoacoustic imaging with integrated delta-sigma beamformer in 28-nm UTBB FD-SOI," *IEEE J. Solid-State Circuits*, vol. 52, no. 11, pp. 2843–2856, Nov. 2017.

[12] J. Lee *et al.*, "A 5.37mW/channel pitch-matched ultrasound ASIC with dynamic-bit-shared SAR ADC and 13.2V charge-recycling TX in standard CMOS for intracardiac echocardiography," in *IEEE ISSCC Dig. Tech. Papers*, Feb. 2019, pp. 190–192.

[13] *IEEE Standard for Information Technology-Telecommunications and Information Exchange Between Systems–Local and Metropolitan Area Networks–Specific Requirements Part 3: Carrier Sense Multiple Access With Collision Detection (CSMA/CD) Access Method and P*, IEEE Standard 802.3, The Institute of Electrical and Electronics Engineers, Inc., New York, NY, USA, 2002.

[14] C. Bulach, U. Bihr, and M. Ortmanns, "Evaluating the influence of the bit error rate on the information of neural spike signals," in *Proc. 19th IEEE Int. Conf. Electron., Circuits, Syst.*, Dec. 2012, pp. 21–24.

[15] E. Cavero, A. Alesanco, and J. Garcia, "Enhanced protocol for real-time transmission of echocardiograms over wireless channels," *IEEE Trans. Biomed. Eng.*, vol. 59, no. 11, pp. 3212–3220, Nov. 2012.

[16] S. Pudlewski and T. Melodia, "On the performance of compressive video streaming for wireless multimedia sensor networks," in *Proc. IEEE Int. Conf. Commun.*, May 2010, pp. 1–5.

[17] J. Wang *et al.*, "Capsule ultrasound device: Characterization and testing results," in *Proc. IEEE Int. Ultrason. Symp. (IUS)*, Sep. 2017, pp. 1–4.

[18] M. Tan *et al.*, "A front-end ASIC with high-voltage transmit switching and receive digitization for 3-D forward-looking intravascular ultrasound imaging," *IEEE J. Solid-State Circuits*, vol. 53, no. 8, pp. 2284–2297, Aug. 2018.

[19] U. Madhow, *Fundamentals of Digital Communication*. Cambridge, U.K.: Cambridge Univ. Press, 2008.

[20] B. Analui, "Signal integrity issues in high-speed wireline links: Analysis and integrated system solutions," Dept. Elect. Eng., California Inst. Technol., Pasadena, CA, USA, Tech. Rep CaltechETD:etd-08092005-100809, 2005.

[21] B. Sklar, *Digital Communications: Fundamentals and Applications*, 2nd ed. London, U.K.: Pearson, 2016.

[22] B. Razavi, "The decision-feedback equalizer," *IEEE Soild-State Circuits Mag.*, vol. 9, no. 4, pp. 13–132, Nov. 2017.

[23] S. M. J. Alam, M. R. Alam, G. Hu, and M. Z. Mehrab, "Bit error rate optimization in fiber optic communications," *Int. J. Mach. Learn. Comput.*, vol. 1, no. 5, pp. 435–440, 2011.

[24] A. M. Mohammad, and M. Hossain, "Analog to sequence converter-based PAM-4 receiver with built-in error correction," *IEEE J. Solid-State Circuits*, vol. 53, no. 10, pp. 2864–2877, Oct. 2018.

[25] J. A. Jensen and N. B. Svendsen, "Calculation of pressure fields from arbitrarily shaped, apodized, and excited ultrasound transducers," *IEEE Trans. Ultrason., Ferroelectr., Freq. Control*, vol. 39, no. 2, pp. 262–267, Mar. 1992.

[26] J. A. Jensen, "FIELD: A program for simulating ultrasound systems," in *Proc. IEEE 10th Nordic-Baltic Conf. Biomed. Imag.*, vol. 34. Mar. 1996, pp. 351–353.

[27] R. E. Ziemer and W. H. Tranter, *Principles of Communication Systems, Modulation, and Noise*. Hoboken, NJ, USA: Wiley, 2014.

[28] R. W. Hamming, "Error detecting and error correcting codes," *Bell Syst. Tech. J.*, vol. 29, no. 2, pp. 147–160, Apr. 1950.

[29] R. Dosselmann and D. Y. Xue, "Existing and emerging image quality metrics," in *Proc. Can. Conf. Elect. Comput. Eng.*, May 2005, pp. 1906–1913.

[30] Z. Wang, A. C. Bovik, H. R. Sheikh, and E. P. Simoncelli, "Image quality assessment: From error visibility to structural similarity," *IEEE Trans. Image Process.*, vol. 13, no. 4, pp. 600–612, Apr. 2004.

[31] M. Razaak, M. G. Martini, and K. Savino, "A study on quality assessment for medical ultrasound video compressed via HEVC," *IEEE J. Biomed. Health Inform.*, vol. 18, no. 5, pp. 1552–1559, Sep. 2014.

[32] A. Rodriguez-Molares, O. M. H. Rindal, J. D'hooge, S.-E. Måsøy, A. Austeng, and H. Torp, "The generalized contrast-to-noise ratio," in *Proc. IEEE Int. Ultrason. Symp. (IUS)*, Oct. 2018, pp. 1–4.

[33] M. S. Patterson and F. S. Foster, "The improvement and quantitative assessment of B-mode images produced by an annular array/cone hybrid," *Ultrason. Imag.*, vol. 5, no. 3, pp. 195–213, 1983.

[34] S. Krishnan, K. W. Rigby, and M. O'Donnell, "Improved estimation of phase aberration profiles," *IEEE Trans. Ultrason., Ferroelectr., Freq. Control*, vol. 44, no. 3, pp. 701–713, May 1997.

[35] J. Poulton *et al.*, "A 14-mW 6.25-Gb/s transceiver in 90-nm CMOS," *IEEE J. Solid-State Circuits*, vol. 42, no. 12, pp. 2745–2757, Dec. 2007.

[36] H. Won *et al.*, "A 0.87 W transceiver IC for 100 gigabit Ethernet in 40 nm CMOS," *IEEE J. Solid-State Circuits*, vol. 50, no. 2, pp. 399–413, Feb. 2015.

[37] B. Garlepp *et al.*, "A 1-10 Gbps PAM2, PAM4, PAM2 partial response receiver analog front end with dynamic sampler swapping capability for backplane serial communications," in *Dig. Tech. Papers Symp. VLSI Circuits*, Jun. 2005, pp. 376–379.

[38] *Calculation of B-Mode Image of Synthetic Fetus*. Accessed: Apr. 30, 2012. [Online]. Available: https://field-ii.dk/?examples/fetus_example/fetus_example.html

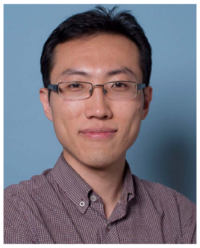

Zhao Chen (M'19) received the B.Sc. degree in microelectronics from Fudan University, Shanghai, China, in 2011, and the M.Sc. degree in electrical and electronic engineering from Imperial College, London, U.K., in 2012. He is currently pursuing the Ph.D. degree in electrical engineering with the Electronic Instrumentation Laboratory, Delft University of Technology, Delft, The Netherlands, with a focus on application-specific integrated circuit (ASIC) design for 3-D medical ultrasound imaging.

His current research interests include analog and mixed-signal electronics, especially for biomedical applications.

Mehdi Soozande (S'18) was born in Larestan, Iran, in 1987. He received the bachelor's degree in electrical engineering from the University of Sistan and Baluchestan, Zahedan, Iran, in 2011, and the master's degree in biomedical engineering from the Tehran University of Medical Sciences, Tehran, Iran, in 2015. He is currently pursuing the Ph.D. degree with the Biomedical Engineering Department, Erasmus Medical Center (Erasmus MC), Rotterdam, The Netherlands.

His main research field is ultrasound beamforming for high-frame-rate 3-D cardiac imaging.

Hendrik J. Vos (M'14) received the M.Sc. degree in applied physics from the Delft University of Technology, Delft, The Netherlands, in 2004, and the Ph.D. degree from the Department of Biomedical Engineering, Erasmus Medical Center (Erasmus MC), Rotterdam, The Netherlands, in 2010.

He was a Postmaster Researcher with the University of Florence, Florence, Italy, and a Contract Researcher of the Petrochemical Industry on cutting-edge ultrasonic solutions. He is currently an Assistant Professor with Erasmus MC. His research interests include acoustical array technology for biomedical imaging in all its aspects: transducers, 2-D and 3-D beamforming, cardiac shear waves, ultrafast Doppler, contrast imaging, and related subclinical and clinical studies.

Dr. Vos received the Dutch NWO-TTW-VIDI Personal Grant in 2018.

Johan G. Bosch (M'07) received the M.Sc. degree in electrical engineering from the Eindhoven University of Technology, Eindhoven, The Netherlands, in 1985, and the Ph.D. degree from Leiden University Medical Center, Leiden, The Netherlands, in 2006.

He performed ultrasound and image processing research with Erasmus University Rotterdam, Rotterdam, The Netherlands, and with Leiden University, Leiden. From 1995 to 2005, he was an Assistant Professor and the Head of the Echocardiography Section, Division of Image Processing (LKEB), Department of Radiology, Leiden University Medical Center. He is currently an Associate Professor and a Staff Member with the Department of Biomedical Engineering, Thorax Center, Erasmus Medical Center (Erasmus MC), Rotterdam, where he is also a Leader of projects on 3-D segmentation and 3-D ultrasound guidance in electrophysiology and participates in several projects, e.g., on 3-D transducer development, 2-D and 3-D carotid imaging, and 3-D transesophageal echocardiography imaging. His research interests include 2-D and 3-D echocardiographic image processing/analyses, transducer development, optimal border detection approaches, geometrical and statistical models, and anatomical and physical knowledge representations for border detection.

Martin D. Verweij (M'10) received the M.Sc. *(cum laude)* and Ph.D. degrees in electrical engineering from the Delft University of Technology, Delft, The Netherlands, in 1988 and 1992, respectively.

From 1993 to 1997, he was a Research Fellow with the Royal Netherlands Academy of Arts and Sciences, Amsterdam, The Netherlands. In 1998, he became an Associate Professor with the Laboratory of Electromagnetic Research, Delft University of Technology, and joined the Laboratory of Acoustical Wavefield Imaging in 2011. His current research interests include dedicated transducer design, beamforming algorithms, and the theoretical modeling and numerical simulation of medical ultrasound.

Dr. Verweij is an Associate Editor of the *Journal of the Acoustical Society of America*.

Nico de Jong (A'97–M'09) received the M.Sc. degree in physics specialized in the field of pattern recognition from the Delft University of Technology, Delft, The Netherlands, in 1978, and the Ph.D. degree in acoustic properties of ultrasound contrast agents from the Department of Biomedical Engineering, Thorax Center, Erasmus Medical Center (Erasmus MC), Rotterdam, The Netherlands, in 1993.

In 2003, he joined the University of Twente, Enschede, The Netherlands, as a part-time Professor. He currently teaches with technical universities and Erasmus MC. He has been a Promotor of 21 Ph.D. students and is currently co-supervising 11 Ph.D. students. Since 1980, he has been a Staff Member with the Thorax Center, Erasmus MC. Since 2011, he has been a Professor of molecular ultrasonic imaging and therapy with Erasmus MC and with the Delft University of Technology, where he has been the part-time Head of the Department of Acoustical Waveform Imaging, since 2015. Over the last five years, he has given over 30 invited lectures and has given numerous scientific presentations for international industries. He has been a Principal Investigator (PI) and the Workpackage Leader of the European and Dutch projects. He has authored 260 peer-reviewed articles. His h-factor is 46 (Web of Science), and he has been acquired over €6 million as a PI or a Co-PI since 2010.

Dr. de Jong is the Organizer of the Annual European Symposium on Ultrasound Contrast Imaging, Rotterdam, which is attended by approximately 175 scientists from universities and industries all over the world. He is on the Safety Committee of the World Federation of Ultrasound in Medicine and Biology, and an Associate Editor of *Ultrasound in Medicine and Biology* and a Guest Editor of the special issues of different journals.

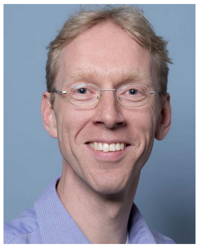

Michiel A. P. Pertijs (S'99–M'06–SM'10) received the M.Sc. and Ph.D. degrees *(cum laude)* in electrical engineering from the Delft University of Technology, Delft, The Netherlands, in 2000 and 2005, respectively.

From 2005 to 2008, he was with National Semiconductor, Delft, where he designed precision operational amplifiers and instrumentation amplifiers. From 2008 to 2009, he was a Senior Researcher with imec/Holst Centre, Eindhoven, The Netherlands. In 2009, he joined the Electronic Instrumentation Laboratory, Delft University of Technology, where he is currently an Associate Professor. He heads a research group working on integrated circuits for medical ultrasound and energy-efficient smart sensors. He has authored or coauthored two books, four book chapters, 15 patents, and over 100 technical papers.

Dr. Pertijs is a member of the Technical Program Committee of the European Solid-State Circuits Conference (ESSCIRC), and also served on the program committees of the International Solid-State Circuits Conference (ISSCC) and the IEEE Sensors Conference. He was a recipient of the ISSCC 2005 Jack Kilby Award for Outstanding Student Paper and the JSSC 2005 Best Paper Award. He received the 2006 Simon Stevin Gezel Award from the Dutch Technology Foundation STW for his Ph.D. research on high-accuracy CMOS smart temperature sensors. In 2014, he was elected the Best Teacher of the EE Program at the Delft University of Technology. He served as an Associate Editor for the IEEE Journal of Solid-State Circuits (JSSC).